

# Computer-aided engineering (CAE) simulation for the robust gating system design: Improved process for investment casting defects of 316L stainless steel valve housing

Ming-Hsiu Ho

Yi Chen Kao

Cheng-Fu Huang

Sheng-Chan Lee

Chien-Wei Chan

Yiin-Kuen Fuh (✉ [michaelfuh@gmail.com](mailto:michaelfuh@gmail.com))

National Central University

---

## Research Article

**Keywords:** CAE, gating system design, investment casting, 316L stainless steel, valve housing, shrinkage defects

**Posted Date:** March 17th, 2021

**DOI:** <https://doi.org/10.21203/rs.3.rs-295542/v1>

**License:** © ⓘ This work is licensed under a Creative Commons Attribution 4.0 International License.

[Read Full License](#)

---

# Abstract

Defects in investment casting will inevitably reduce the lifetime and degrade the casting quality and increase manufacturing costs, accordingly. In particular, shrinkage porosity was numerically conducted, and a retained melt modulus model was implemented to analyze highly probable regions. The proposed casting schemes of gating designs are compared by quality of casting (shrinkage porosity) and practical feasibility in terms of small hole drilling machinability. The purpose of this study was to determine the feasible plan with the lowest PES (percentage of elements with shrinkage porosity) while promoting the near net shape casting with minimum machining cost and increase material usage. Virtual thermodynamical sensors were adopted in the simulations to indicate the impacts of different gating system of pattern assembly on the cooling gradient and direction of solidification. The best-case scenario of investment casting conditions was chosen to fabricate valve housing in an investment casting foundry. Experimental results of X-ray image differentiated nearly none of the pernicious defects that typically occurred with proposed casting, authenticating the proposed scheme's efficacy accordingly.

## Introduction

Industrial meters are widely used in various sectors to measure velocities, flow, pressure, etc., such as liquid valve and gas valve. These systems are subject to high pressure or even corrosive environments and must maintain perfect sealing performance, which means that the parts have an increased risk of corrosion and leakage and require regular maintenance. The valve housing is usually manufactured via casting; nevertheless, the mechanical strength will substantially reduce by casting defects and sealing performance of the component. Unpredictable breakage of the valve housing may cause severe damage if toxic substances leak or cause economic loss or process instability. [1-4]

High accuracy in creating products with smooth surfaces and sophisticated geometry usually produced by investment casting [5-10]. The production process of valve housing via investment casting is exceptionally complicated; part of the reason is that the shrinkage during the casting process is nonlinear [11,12]. The casting processes of 316L valve housing have been simulated with the numerical method. Four types of gating systems of pattern assembly are designed and analyzed. In the initial scheme, a closer casting pattern assembly method is used, and there is some shrinkage porosity found on the surface of the simulation result and trial casting. Minimizing the PSE closely related to the gating system is the casting gating system's eventual optimization goal [13,14]. The feeding system is a structure for storing the molten material to compensate for the possible shrinkage in the solidification phase during the casting process [15–17].

Technologically advanced computer-aided engineering (CAE) simulation and the nondestructive testing technology are desirable for the design alternative. They possess many advantages such as improving quality, reducing cost, shortening development schedule. [18-20] CAE simulation is the most efficient and profitable technology from the perspective of quality and defect prediction for analyzing and evaluating the quality and defects of casting products. [21,22] Many previous casting research methods have

chosen trial-and-error ways, often unreliable, time-consuming, and costly. One of the fundamental dilemmas is that it's arduous to build reliable predictions about the casting defects arrangement because we cannot inspect the flow of molten metal in the cavity and the tendency of solidification. [8,12,22] Using CAE software can predict the scope and the approximate number of defects that may be formed during the casting process and the direction of solidification. A lot of development time and cost compared to traditional trial-and-error methods can be minimized. Manufacturers yield, verify, examine and improve the design schemes assisted by CAE simulation technology.

Finally, we will use actual trial casting photos and X-ray inspection to verify that the solution has avoided undesired casting defects.

Fig. 1. shows the simple size and front, back view of the industrial meter body we want to produce. The Schematic diagram of the component is shown in Fig. 1. (a) and Fig. 1. (b)(c) shows the Front-view and back-view of the valve housing solid model. In this research work, a square component with three screw holes. This component has applications in various industries. The weight of casting is approximately 5.23 kg, and the material used is stainless steel (316L).

Fig. 2. illustrates shrinkage porosity observed at the surface of meter body housing manufactured via investment casting. During the solidification process, accurate predictions related to the percentage of elements with shrinkage defect (PES) should be eliminated. Fig. 2 (a)(b) presents photographs of frequently encountered casting defects in experiments. The key reasons can be attributed to the following: (1) The isolated retained melt during solidification resulted from the insufficiently filled molten metal from runners. The shrinkage porosity defects can be formed. (2) A severe temperature gradient occurred at a specific region of a large flat surface during the casting process. Thereby molten iron overflow causes the wrinkled surface defects of the valve housing. (3) The geometry dependent solidification property of the corner screw hole with the highest volume to surface ratio resulted in isolated residual melts. PES value was significantly increased.

Investment casting is an ancient casting process by utilizing losing wax and ceramic shell mold made of mullite slurry, zircon slurry, binder, and other associated materials. The typical investment casting processes include wax injection, wax pattern assembly, stuccoing, losing-wax, pouring, mold-breaking, and sandblasting. There are machining, heat treatment, and surface treatment in the post-processing stage according to casting requirements. Multiple factors such as equipment-related, processing-related, materials-related, and shell mold-related are positively correlated in the routinely exercised process flow. Therefore, investment casting has a complicated and lengthy manufacturing system with the primary process, as illustrated in Fig. 3.

## Materials And Methods

Fig. 4. displays an illustrated schematic with the original scheme used to cast the valve housing, where molten steel poured into the sprue cup and flowed through the lateral runner to the mold cavity. The cavity's initial air was exhausted from the vent hole to liberate the gating system's pressure. The

dimensions of the gating system were showed in Fig. 4. In our CAE simulations, we selected the trial conditions in Table 1., which are widely used in the fabrication of investment casting in our trial casting.

Table 1. Trial casting and simulation conditions for every casting projects

Casting material	Pouring temperature (°C)	Shell mold temperature (°C)	Shell mold thickness (mm)
316L	1680	1180	6

Fig. 5. respectively present interpretations of the gating systems in Case A, Case B, Case C, and Case D. To ensure a reasonable comparison, all numerical simulations of the casting schemes in Fig. 5. were produced using the same conditions in real trial casting. Case A and C have similar assembly patterns, so do CASE B and D. Case C and D are the version of Case A and B to extend the casting distance for adding ceramic core to avoid the difficulty of processing the inner hole of the valve housing. Extending casting distance is designed for placing ceramic cores in the wax model. In Case of D, the outer screw holes are additionally filled in, and the screw holes are processed after casting to avoid defects on the inner side of screw holes. The brown color shape in Case C and D are CAE models of ceramic cores.

Fig. 6. shows the predicted defect regions that appeared by the solidification shrinkage. The modulus method in C3P indicates these shrinkage defect areas. In light of the casting theory, the ununiformed cooling temperature areas usually cause shrinkage defects. It is considering to avoid those defects is what a good pattern of assembling needs. Fig. 6. (a) displays the PES distributions of the gating system in Case A. Shrinkage porosity appeared inside the ring at the front side of casting and the inner side of the screw hole, as shown in Fig. 7. (a). It can be attributed to the tangible that the geometric thickness and cooling rate around the screw hole are higher than the screw hole itself during the cooling phase. Therefore, the molten metal in the riser cannot supplement the screw hole.

Fig. 6. (b) presents the PES distributions of the gating system under Case B as the pattern's front view. Under Case B, the combination of pattern with the assembly method of placing the thick side of the casting in the middle diminished the PES values observed in the ring and the part near the screw hole in Case A. However, we reduced the rate of shrinkage by changing the assembly method.

Fig. 7. shows a graph of the way of pattern assembly versus the percentage of shrinkage elements and indicates that the shrinkage percentage of the casting will be reduced by nearly 45% with the different assembly methods. Changing the placement method and placing the thick side of the casting in the middle of the pattern can make the solidification trend more continuous. The feeding function of the runner can be better. The area where the isolated liquid region is reduced from Case A to B and the location where shrinkage porosity occurs will also be reduced.

Fig. 8 (a) illustrates the shell mold's cracking during trial casting in Case A for real trial casting photograph, as indicated in the red ellipse inset. One of the attributing reasons for the shell mold cracking is the unanticipated change of the velocity magnitude. The corresponding simulated results in Fig. 8. (b) show the velocity magnitude higher than 2500mm/s in red rectangle inset, and magnify view reveals the maximum value can exceed 2850mm/s. A similar trend was also observed in Fig. 8. (c) pressure magnitude can locally accumulate 1.11 MPa in red rectangle inset. Besides, the precipitous gradient of the pressure and velocity magnitude (velocity gradient is about 1025.5 1/s, the pressure gradient is about 0.015 MPa/mm) has a similar position with the cracking part of shell mold in Fig. 8. (a).

Fig. 9. illustrates shell mold temperature with time in Case B with measured temperature with a thermal camera (solid line) and simulated temperature (dotted line). Generally speaking, the simulated temperature higher than the measured temperature, and the temperature difference was in the range of 100 -200°C for P1-P3 positions. The possible discrepancy was mainly attributed to forced convection of the wind in the open space, measurement error due to the heat photography distance.

Fig. 10. shows the expected defect areas from Case A to Case D occurred by the solidification shrinkage. The results of Fig. 10. (a)(b) have been discussed in Fig. 6. Fig. 10. (c) shows the Case C PES distributions as the front view of the pattern. Casting defects appeared inside the ring at the front side of casting and the inner side of the screw hole, as shown in Fig. 10 (c). These areas with shrinkage defects in Case C are similar to Case A's location while extensively distributed and can be primarily attributed to the solidified tendency to become less continuous due to the distance between the castings being extended. As the distance between the castings becomes more extensive, the heat preservation effect caused by heat radiation is also reduced, causing the solidification tendency to become worse. It also causes the influence of runner feeding in Case C to be worse than the Case A.

Fig. 10. (d) shows the Case D PES distributions as the front view of the pattern. The phenomenon observed between Case B & D is similar to Case A & B. The reason for the slight increase in the percentage of shrinkage defects is the extending of the casting distance.

Fig 11. Informs the shrinkage porosity prediction in Case A to Case D. When the distances between castings increase in patterns, the percentages of elements with shrinkage increase (Case C has 5% more PES than Case A, and Case D has 20% more than Case B). Though Case D has more PES, it can prevent the shrinkage defects on the inside of the screw hole, and we must choose the final case in Case C or D due to avoid the difficulty of processing the inner hole on the casting by adding ceramic cores.

Fig. 12. (a)-(d) reveal the positions of the virtual thermo-dynamic sensor (VTDS) placed in each gating systems: (a) Case A, (b) Case B, (c) Case C, (d) Case D. In the schematic diagram, marked the VTDS from number 1 to 5 on the red dots. The VTDS were placed in the center of the runner, gate, and structure of the valve housing, where there can describe the solidification trend of the entire casting clearly.

Fig. 13. (a)–(d) presents temperature alternations of molten metal at the VTDS in different casting scheme as a time function: (a) Case A, (b) Case B, (c) Case C, (d) Case D. The results in Fig. 17 illustrated

the following significant findings: (1) The time required for the molten iron from the liquidus temperature (1412 °C) drops to the solidus temperature (1338 °C) of the alloy 316L at point 4 & 5 was as follows: 150 s (Case A) and 175 s (Case B), as shown in Fig. 13 (a) and (b). This time discrepancy demonstrates that the pattern assembly method will delay solidification for 25 s and allow enough molten metal flow into the mold cavity. (2) The time required for the molten iron from the liquidus temperature (1412 °C) drops to the solidus temperature (1338 °C) of the alloy 316L at point 4 & 5 was as follows: 100 s (Case C) and 138 s (Case D), as shown in Fig. 13 (c) and (d). This time discrepancy demonstrates that the pattern assembly method will delay solidification for 38 s and allow enough molten metal flows into the mold cavity. (3) We can also find that Case C and D's cooling rate at points 4 and 5 is faster than that of Case A and B, resulting in a slight drop in Case C and D's casting quality compared to Case A & B. It can be approved in Fig.13. (4) The cooling rate of point 1, 2, and 3 are slower than point 4,5 in Fig. 13., it proves that when the casting starts to solidify, the molten metal can continue to be fed into the casting due to the higher temperature of the runner and pouring cup, reducing the generation of shrinkage defects. The slower cooling rate significantly reduced the likelihood of shrinkage porosity and shrinkage cavity

Fig. 14. (a)(c) illustrate the predicted spots of shrinkage defect distribution on the workpiece's surface in simulation. The areas where shrinking defects formed are shown in blue areas. Fig. 14. (b)(d) reveals the casting defects on the surface of the valve housing in the photograph. These effects can be attributed to the placement method of the assembly pattern. In Case C, the thicker part of the casting was placed on the tree's outer side, where a larger cooling rate would be. An isolated liquid region occurred at the rapidly cooling place and caused shrinking porosity.

Fig. 15. present some of the cavitation defects on the surface manufactured by investment casting, including microporous forming due to shrinkage between the corner screw hole's inner side due to geometric inequality of the casting. Designers must have the ability to make precise predictions concerning shrinkage during the cooling process to develop solutions to eliminate the defects.

Ceramic cores were utilized in our Cases C, D because inner holes are hard to be processed. However, the ceramic cores were easily broken while molten iron pouring in when the first trial casting in Case C and Case D. Ceramic core fracturing problem caused valve housing shape deformed as shown in Fig. 16. The best solution for this problem is to change the composition of the ceramic cores, and the results are satisfactory.

Fig. 17. (a) illustrates wrinkled surface defects in shell mold cracks caused by a high-temperature gradient in the solidification process during trial casting in Case D for real trial casting photograph. Simulation results in regions with a large temperature gradient (Case D) coincides in the same position with some surface defects on actual casting. After pouring 645 seconds in simulation, the orange rectangle inset's temperature can rise from 1037°C to 1178°C within a 3cm distance shown in Fig. 17. (b) and the temperature gradient is about 47°C/cm. The red rectangle inset in Fig. 17. (c) reveals the temperature after pouring 364 seconds can rise from 1059°C to 1161°C within 3cm distance, and the temperature gradient is about 34 °C/cm. The large temperature gradient may cause the casting to expand

unevenly, which will cause some micro cracks on the surface of the shell mold and cause the wrinkled surface defects of the casting.

Fig. 18. According to Case D, submit photographs of trial casting to certify the simulation results with a filled corner screw hole: Fig. 18. (a) simulation model of Case D without surface defects, Fig. 18. (b) the finished product of casting after machining, Fig. 18. (c)(d) enlarged images showing the perfect screw hole of Case D. After machining, the inner wall of the screw hole in Case D is perfect without defects, which meets customer needs for this casting. There aren't any apparent shrinkage defects in the finished product, as revealed in Fig. 15(b)–(d). Moreover, no black spots in the X-ray photograph detected inside the valve housing by nondestructive testing, as shown in Fig. 18. (e)–(f). The quality of the trial stainless steel (316L) valve housing from Case D contributes convincing evidence supporting the effectiveness of our casting strategy of the valve housing.

Fig. 19 illustrates shell mold temperature with time in Case D with measured temperature with the thermal camera (solid line) and simulated temperature (dotted line). Generally speaking, the simulated temperature lower than the measured temperature, and the temperature difference was about 100°C for P1-P3 positions. The possible discrepancy was mainly attributed to the difference in environmental conditions in the open space. The idealization of the environment temperature setting in simulation causes the shell mold temperature to drop rapidly at the cooling process beginning after the distance between the castings extended.

To validate the accuracy of simulation results, the valve housing was investment casted in the casting factory using the CAE derived casting parameters. X-ray was used to evaluate the adequacy of optimized casting conditions in reducing or avoiding casting defects. Fig. 20. (b) presents a photograph of the wax pattern. Fig. 20. (c) presents a front-view of casting at the left side and back view of casting at the right side without surface defects of the final casting under Case D. Fig. 20. (d) demonstrates X-ray images of the casting results, which prove the efficacy of the casting parameters under Case D. No black spots in the X-ray photograph were detected inside the valve housing under Case D, as shown in the image in Fig. 20. (d). The quality of the trial stainless steel (316L) valve housing from Case D contributes convincing evidence supporting the effectiveness of our casting strategy of the valve housing

## Conclusions

In this study, the numerical simulations based on the modulus method were used to predict where and how shrinkage defects can form in stainless steel (316L) industrial meter housing for the valve. Our results from the past casting experience, preparatory simulations, and experiments were used to formulate four casting schemes for simulation. The plan with the smallest PES was selected for the final gating system. We set virtual TDSs in every casting system simulation to characterize the cooling rates and solidification directions in different casting regions after pouring. Our simulation results illustrate that the gating system (Case D) extended could reduce most casting defects.

Moreover, Case D's filling the screw hole can eliminate the shrinkage defects after processing on the inner side of the screw hole. At the same time, the design of adding ceramic core to Case D can avoid the problem of processing the inner hole, so we can perfectly meet the requirements of the client. We then applied the casting conditions as the simulation set to manufacture a meter body for a real casting valve. X-ray photographs illustrate that the suggested gating system and prearranged casting conditions removed most of the destructive casting defects typically related to this casting method. The strategy revealed in this paper provides a helpful reference for the investment casting of the valve body from the aspect of quality and cost-effectiveness.

## **Declarations**

### **1. Funding**

This research is supported by the project funded by GlobalTek Fabrication Co., Ltd. in cooperation with National Central University.

### **2. Conflicts of interest/Competing interests**

We declare that we have no financial and personal relationships with other people or organizations that can inappropriately influence our work, there is no professional or other personal interest of any nature or kind in any product, service and/or company that could be construed as influencing the position presented in, or the review of, the manuscript entitled.

### **3. Availability of data and material**

The authors confirm that the data supporting the findings of this study are available within the article.

### **4. Code availability**

Not applicable.

### **5. Authors' contributions**

All authors contributed equally to the generation and analysis of experimental data, and the development of the manuscript.

### **6. Ethics approval**

This article does not contain any studies with human participants or animals performed by any of the authors.

### **7. Consent to participate**

All authors declare that have agreed for authorship, have read and approved the manuscript, and have given the consent for submission and subsequent publication of the manuscript.

## 8. Consent for publication

All authors are consenting to publish this article with its included data in The International Journal of Advanced Manufacturing Technology and approve its final version.

## References

1. Huang PH, Cheng CY, Huang WJ, Chou CSh (2020) Optimal design of investment casting system for toothed chain joint: computer simulations and experimental verification. *Int J Adv Manuf Technol* 106:1931–1943
2. Kuo JK, Huang PH, Lai HY, Chen JR (2017) Optimal gating system design for investment casting of 17-4PH stainless steel enclosed impeller by numerical simulation and experimental verification. *Int J Adv Manuf Technol* 92:1093–1103
3. Wu M, Augthun M (2001) Application of laser measuring, numerical simulation and rapid prototyping to titanium dental castings. *Dent Mater* 17:102–108
4. Kuo JK, Huang PH, Guo MJ (2017) Removal of CrMo alloy steel components from investment casting gating system using vibration excited fatigue failure. *Int J Adv Manuf Technol* 89:101–111
5. Huang PH, Shih KL, Lin HM, Chu CI, Chou CS (2019) Novel approach to investment casting of heat-resistant steel turbine blades for aircraft engines. *Int J Adv Manuf Technol* 104:2911–2923
6. Huang PH, Kuo JK, Guo MJ (2017) Removal of Cr Mo alloy steel components from investment casting gating system using vibration excited fatigue failure. *Int J Adv Manuf Technol* 89:101–111
7. Zhi XH, Han YJ, Yuan XM (2015) Casting process optimization for the impellor of 200ZJA slurry pump. *Int J Adv Manuf Technol* 77: 1703–1710
8. Huang PH, Wang BT, Chen YT (2014) An effective method for separating casting components from the runner system using vibration-induced fatigue damage. *Int J Adv Manuf Technol* 74: 1275–1282
9. Hou YH, Cheng ZQ, Feng WC, Liu BS (2007) Using Procast to forecast and analysis of the shrinkage porosity and its technical optimization swaminathan. *China Water Transport* 7(3):67–69
10. Huang PH, WuWJ, Shieh CH(2016) Compute-aided design of low pressure die-casting process of A356 aluminum wheels. *ApplMech Mater* 864:173–178
11. Dong YW, Li XL, Zhao Q, Yang J, Dao M (2017) Modeling of shrinkage during investment casting of thin-walled hollow turbine blades. *J Mater Process Technol* 244:190–203
12. Wang PH, Sun JP, Dong AP, Shu D, Zhu GL, Sun BD (2018) An optimization method of gating system for impeller by RSM and simulation in investment casting. *Int J Adv Manuf Tech* 98:3105-3114
13. Hardin RA, Choi KK, Gaul NJ, Beckermann C (2015) Reliability based casting process design optimization. *Int J Cast Met Res* 28(3): 181–192

14. Bu K (2017) Research on the influence of structure parameters on the fractional shrinkage of wheel shape casting. *Int J Adv Manuf Technol* 93:3933–2942
15. Jin J, Liu CH, Lai XM, Li F, He B (2017) Bayesian network approach for ceramic shell deformation fault diagnosis in the investment casting process. *Int J Adv Manuf Technol* 88:663–674
16. Sata A, Ravi B (2017) Bayesian inference-based investment casting defect analysis system for industrial application. *Int J Adv Manuf Technol* 90:3301–3315
17. Wang JQ, Fu PX, Liu HG, Li DZ, Li YY (2012) Shrinkage porosity criteria and optimized design of a 100-ton 30Cr<sub>2</sub>Ni<sub>4</sub>MoV forging ingot. *Mater. Des.* 35:446-456
18. Li DZ, Campbell J, Li YY (2004) Filling system for investment cast Ni-base turbine blades. *J Mater Process Technol* 148:310–316.
19. Hu BH, Tong KK, Niu XP, Pinwill I (2000) Design and optimization of runner and gating systems for the die casting of thin-walled magnesium telecommunication parts through numerical simulation. *J Mater Process Technol* 105:128–133.
20. Zhang XP, Chen G (2005) Computer simulation of the solidification of cast titanium dental prostheses. *J Mater Sci* 40:4911–4916
21. Kwon HJ, Kwon HK (2019) Computer aided engineering (CAE) simulation for the design optimization of gate system on high pressure die casting (HPDC) process, *Robot Comput Integr Manuf* 55:147-153
22. Kim ES, Park JY, Kim YH, Lee KH (2009) Evaluation of diecasting mold cooling ability by decompression cooling system, *J. Korea Foundry Soc* 29:238–243

## Figures

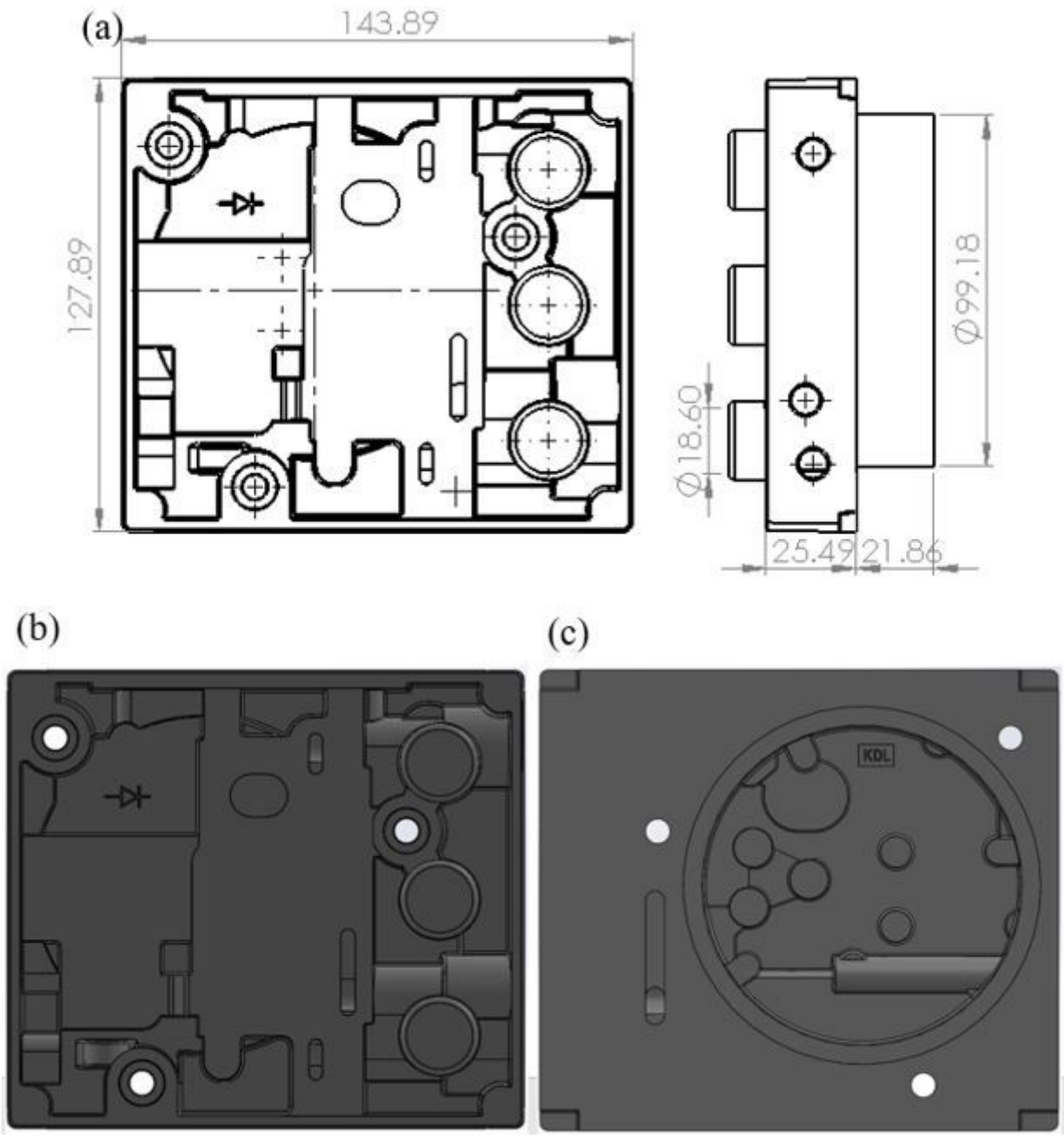


**Figure 1**

(a) casting diagram of valve housing component and size information. (all units in mm) (b) front-view. (c) back-view.

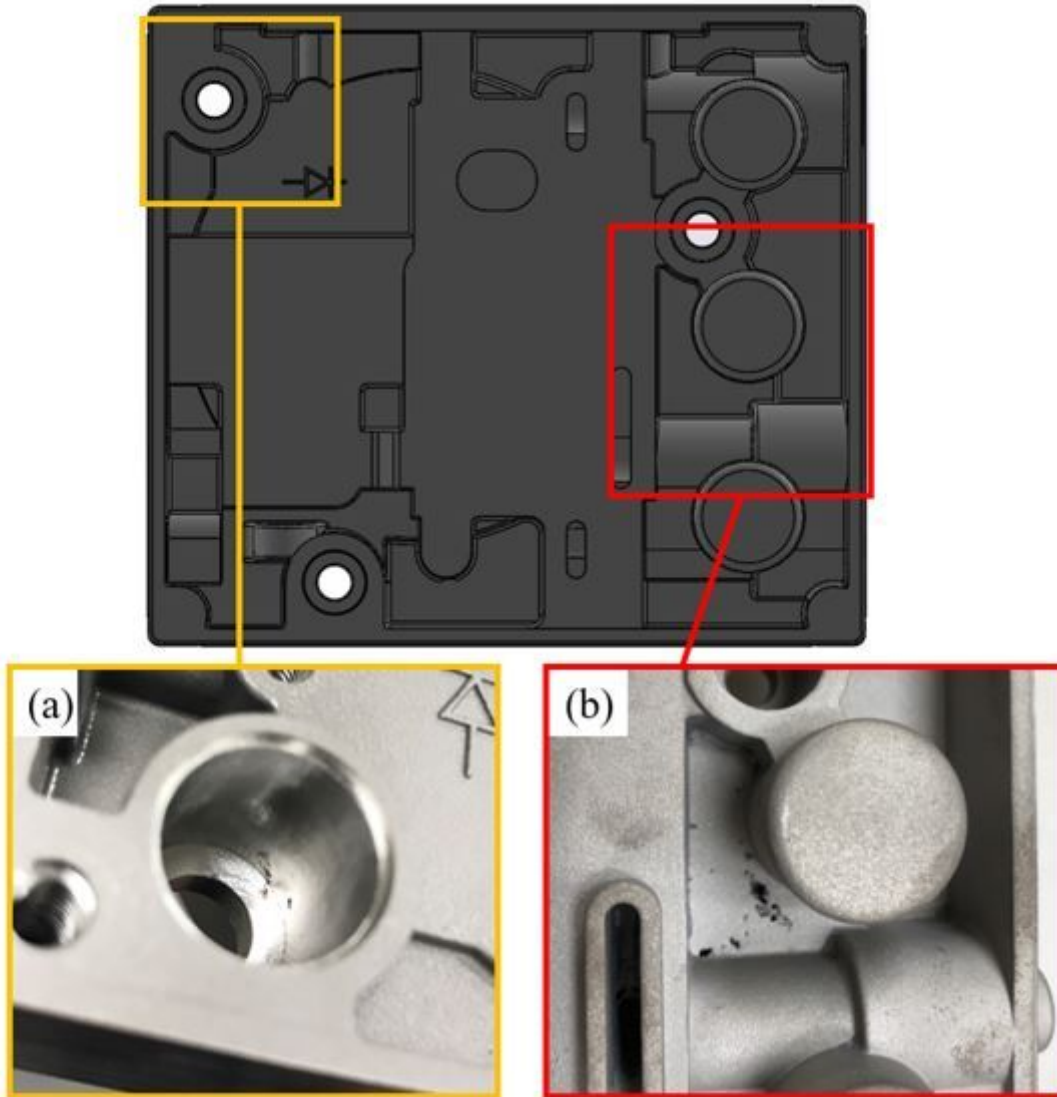


**Figure 2**

Common casting defects in the valve housing. (a) Photography of shrinkage porosity on the inner wall of the screw hole before machining. (b) Photography of shrinkage porosity on the surface of the valve housing.

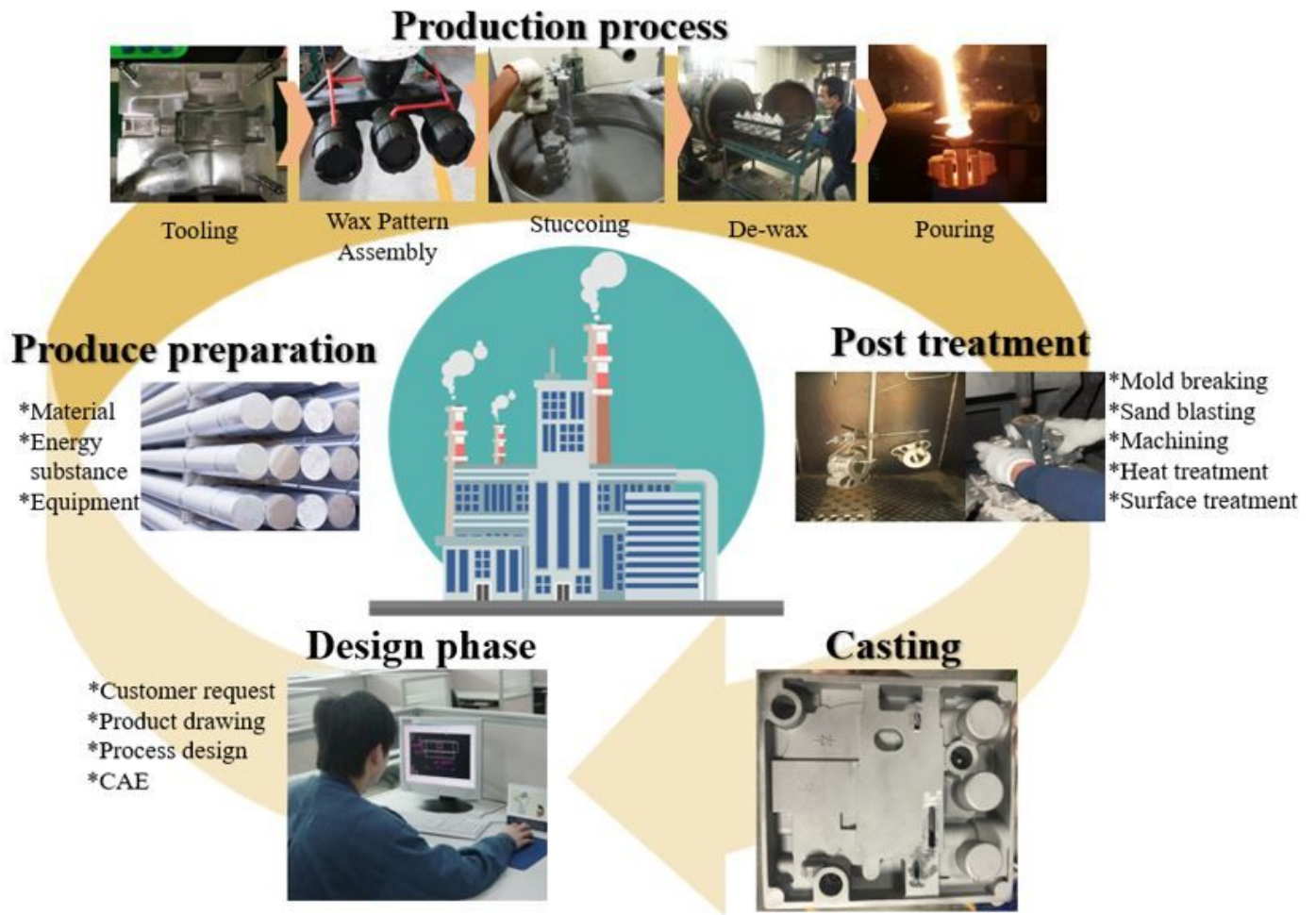


**Figure 3**

Investment casting process.

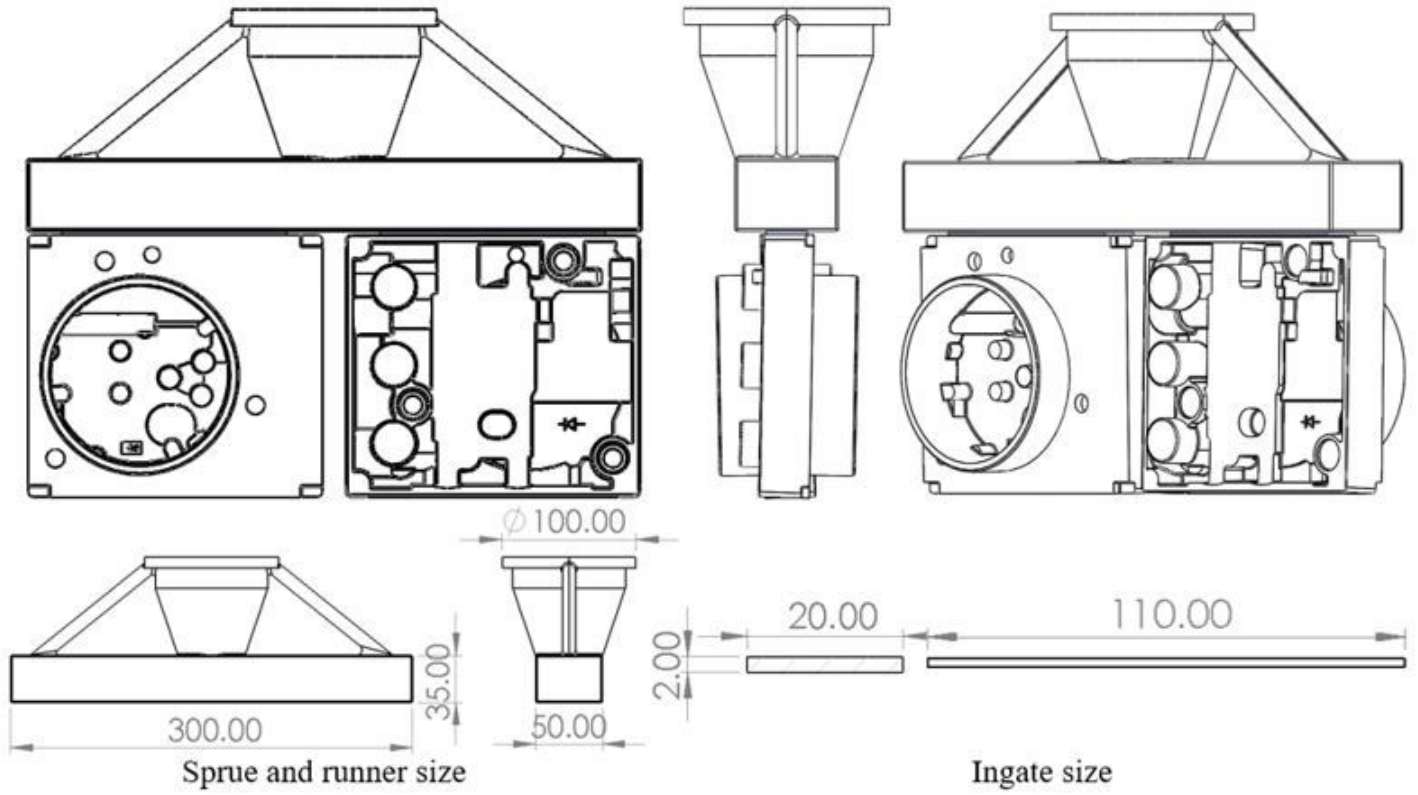


**Figure 4**

Original casting design schematic. (sprue, runner, and gate size)

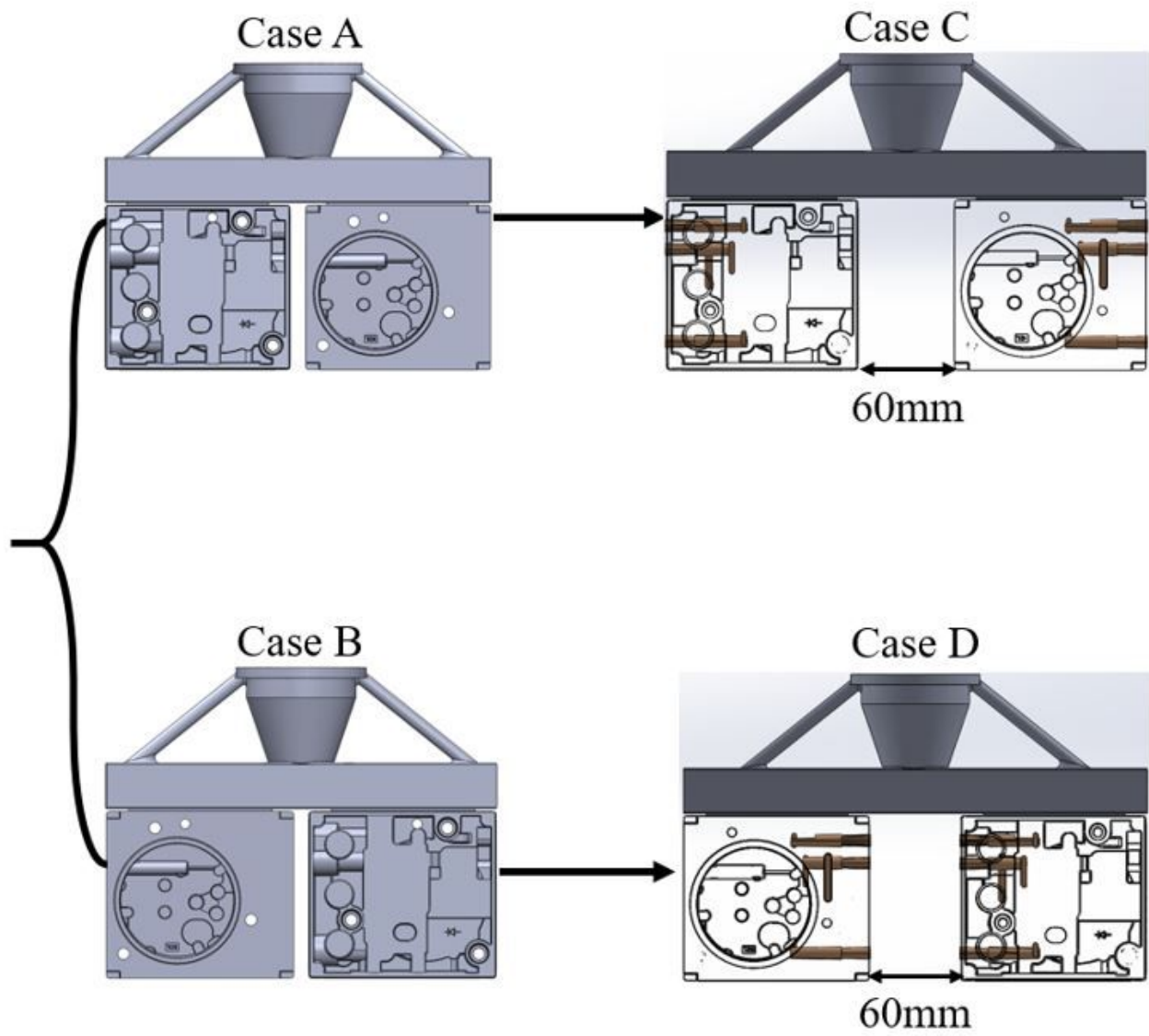


Figure 5

Illustrations of the casting pattern

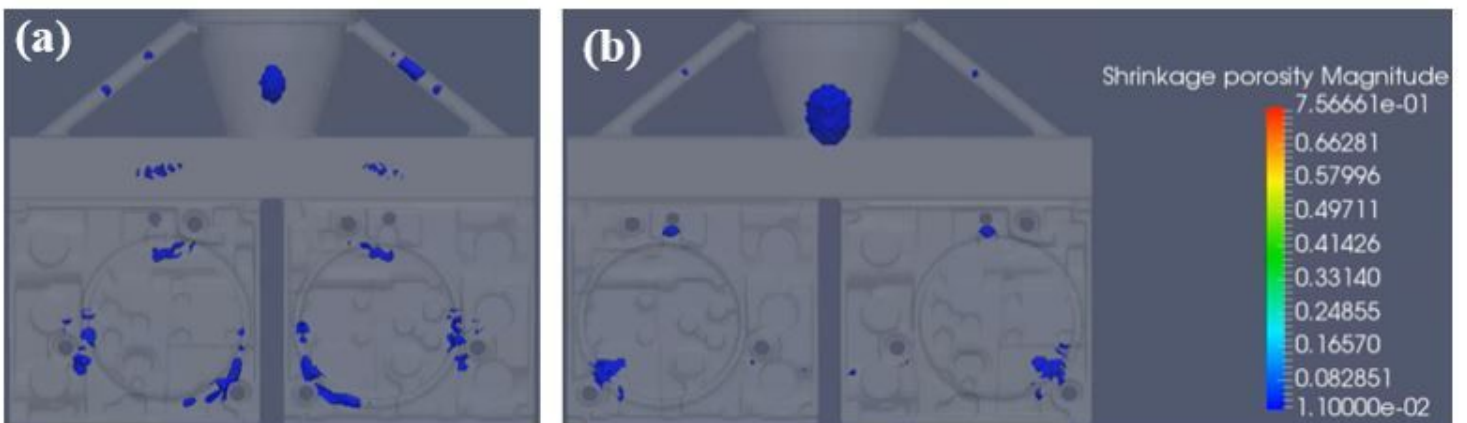
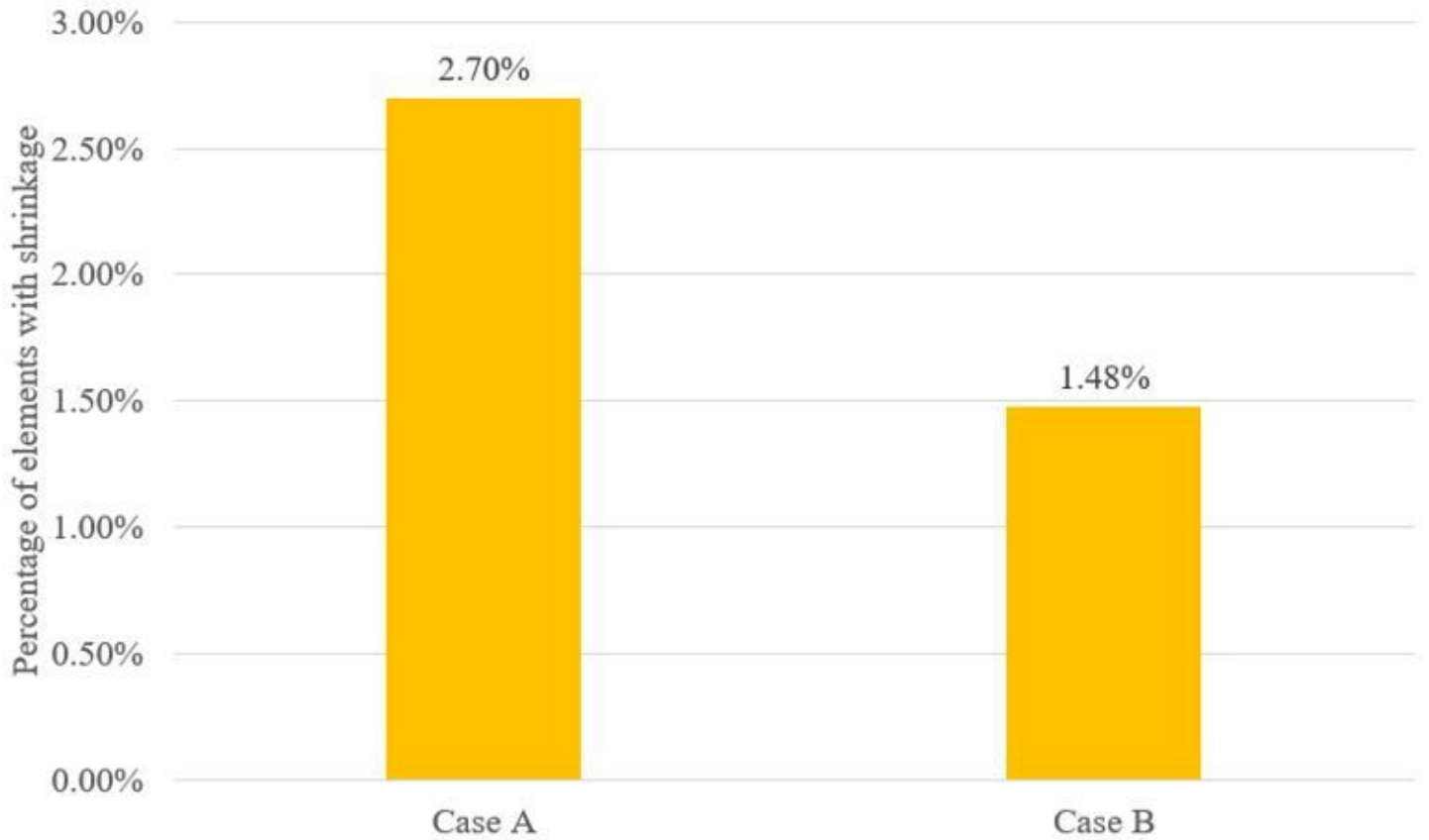


Figure 6

Original process (Case A and B) simulation results for shrinkage porosity prediction as to the front view  
(a) Case A. (b) Case B



**Figure 7**

Comparison of Case A and B in shrinkage porosity prediction

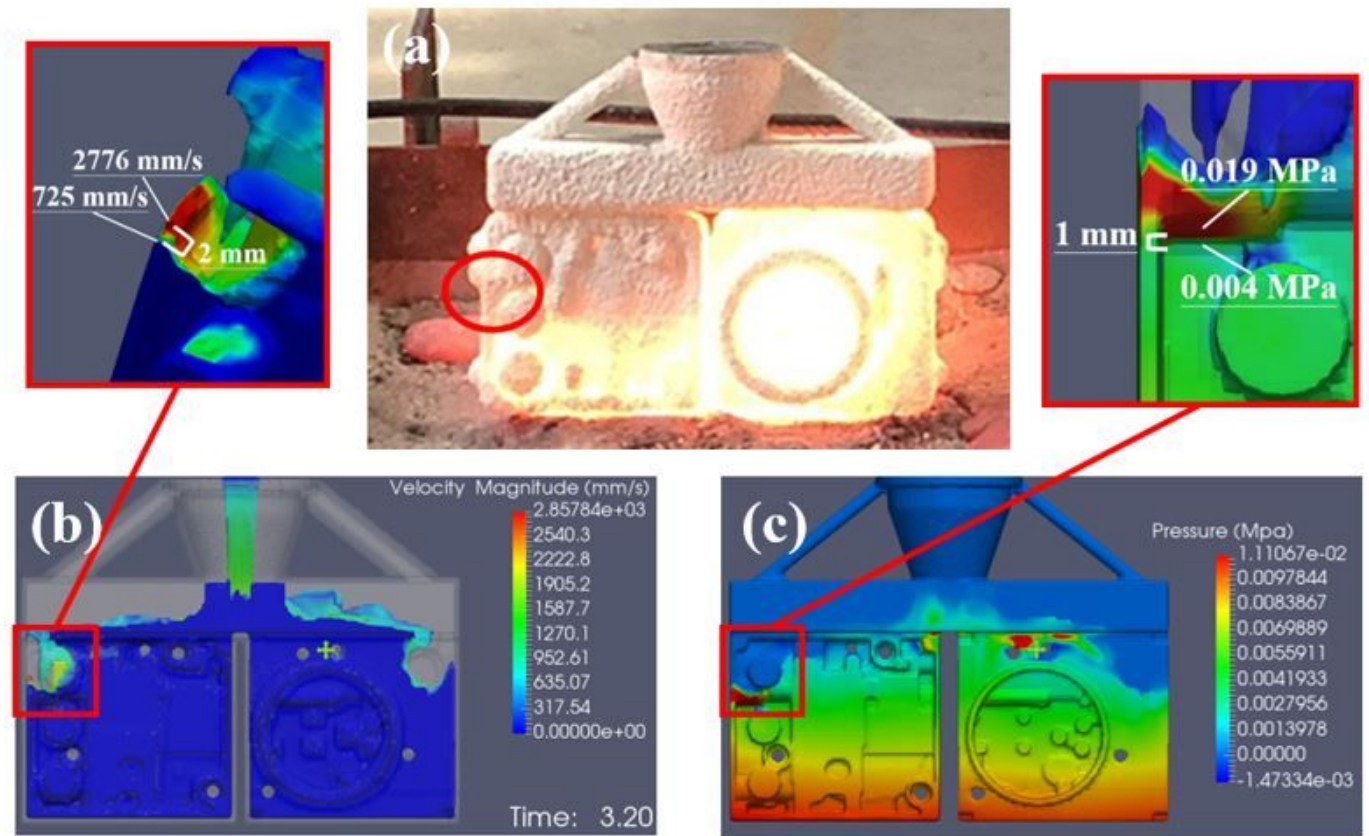
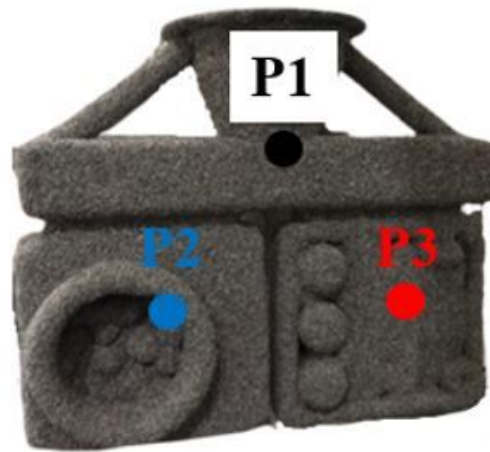


**Figure 8**

Case A encountered the shell mold cracking during trial casting. (a) real trial casting photograph. Corresponding the simulated results (b) velocity magnitude. (c) pressure magnitude.



Case B shell temperature T-t diagram

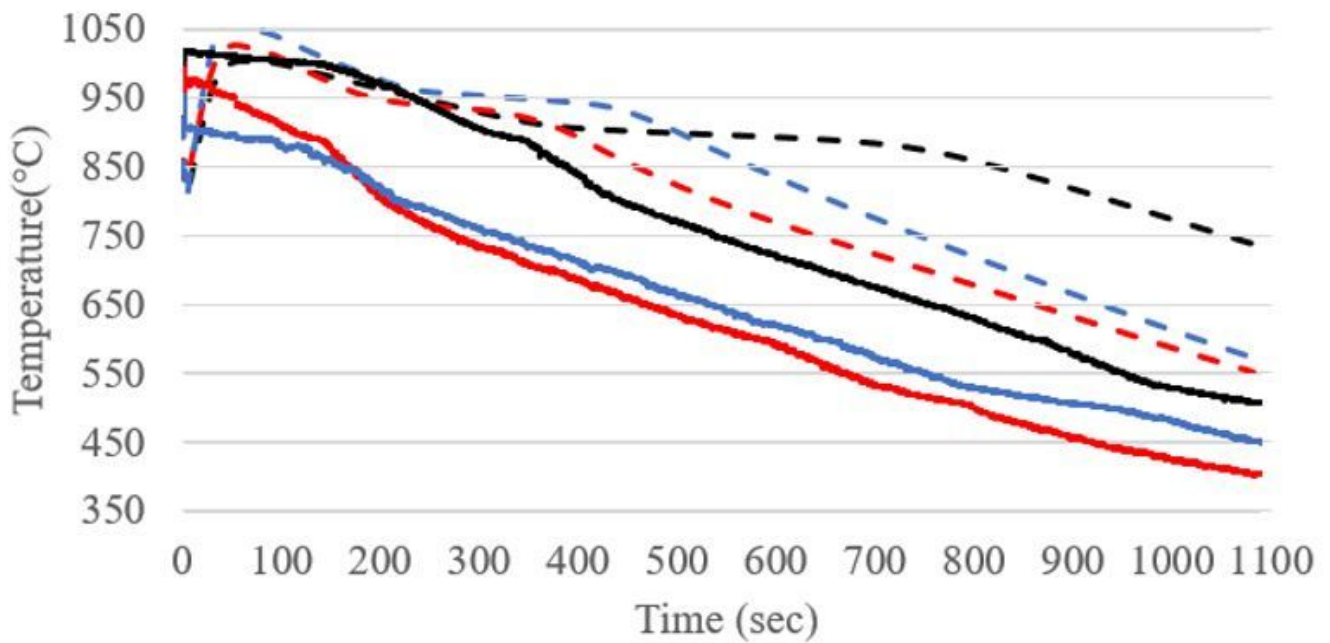
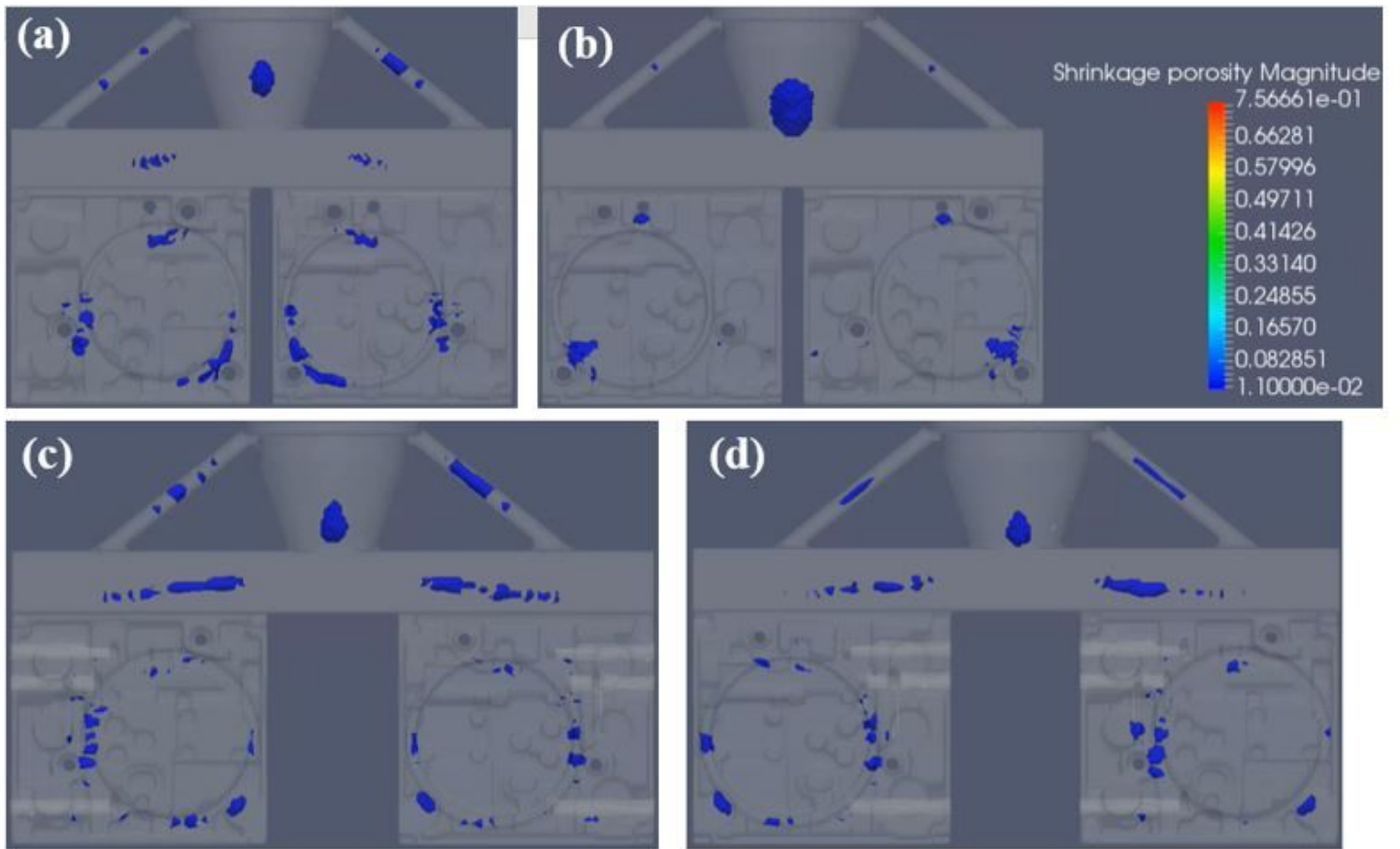


Figure 9

Case B shell mold temperature with time during the solidification process in three different positions, i.e., P1 in central of the runner, P2 in central of the front side of the casting shell mold, and P3 in mid of the backside of the casting shell mold. Actual temperature measured with a thermal camera (solid line) and temperature predicted in simulation result (dotted line)



**Figure 10**

Shrinkage porosity prediction for all simulation schemes. (a) Case A. (b) Case B. (c) Case C. (d) Case D.

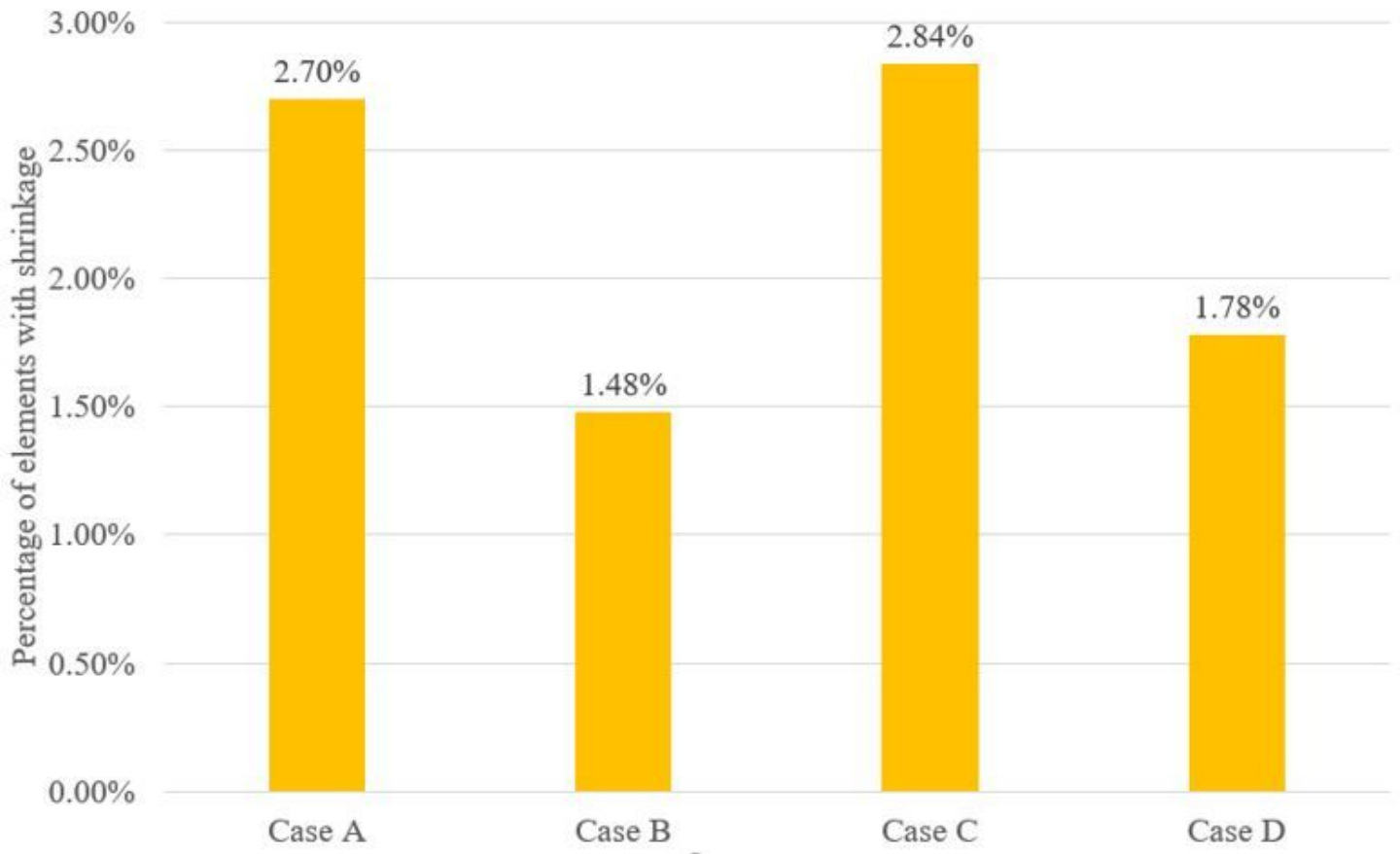


**Figure 11**

Comparison of Case A-D in shrinkage porosity prediction

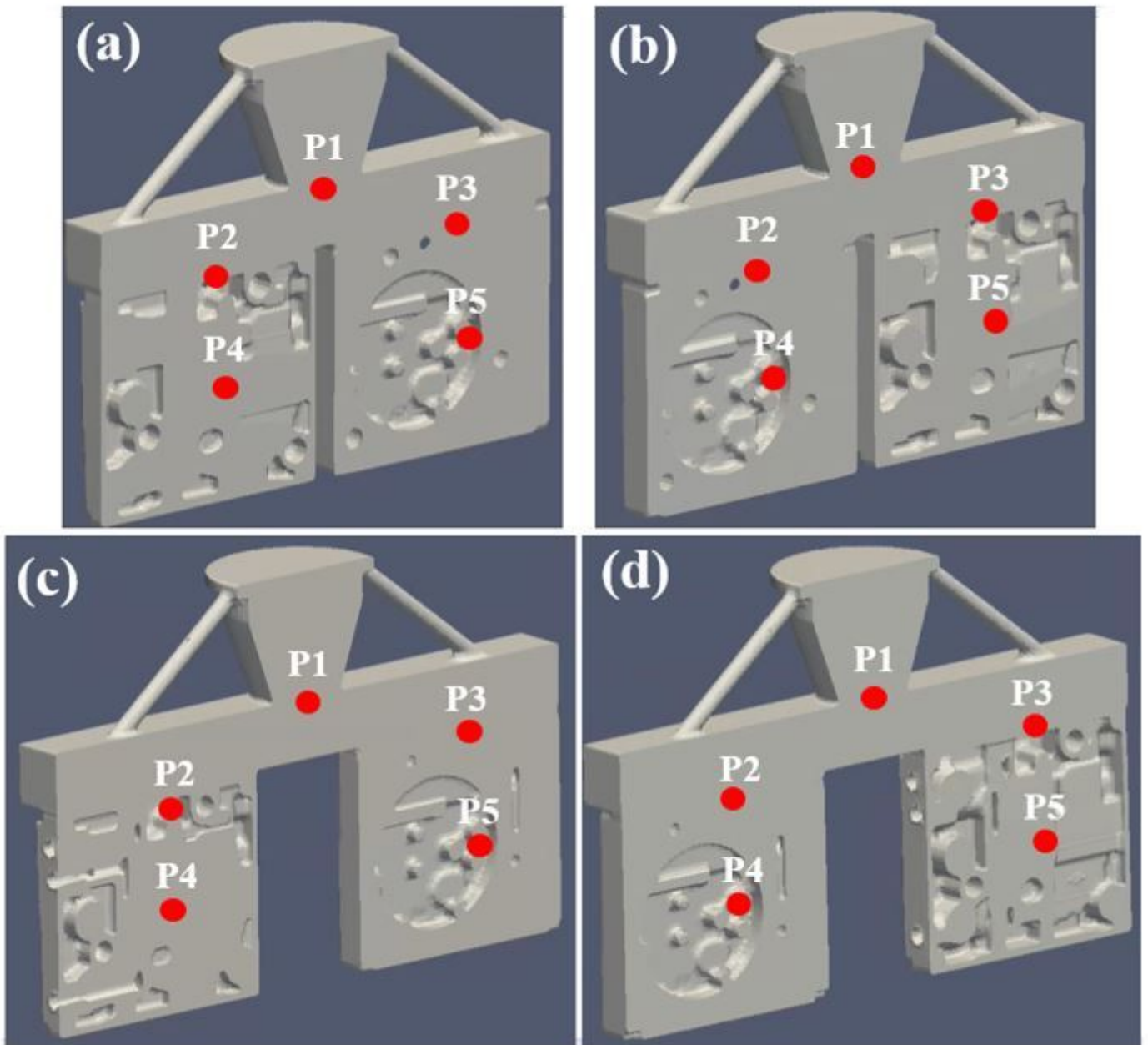


**Figure 12**

Schematic illustrates the locations of the virtual thermo-dynamic sensor (VTDS) in the gating system and casting. (a) Case A. (b) Case B. (c) Case C. (d) Case D.

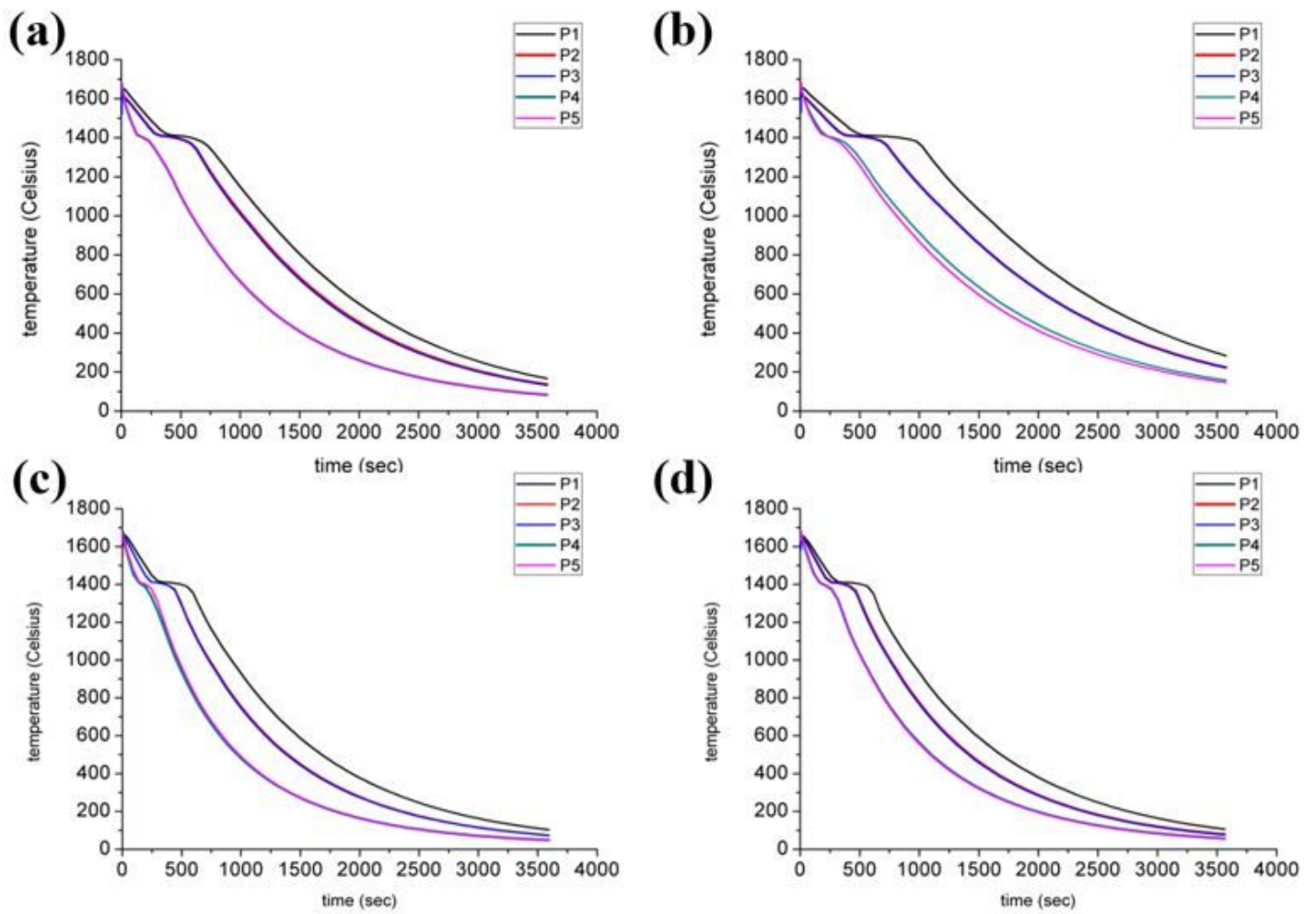


**Figure 13**

The temperature alternations of molten metal at the VTDS (virtual thermodynamic sensors) over time. (a) Case A. (b) Case B. (c) Case C. (d) Case D.

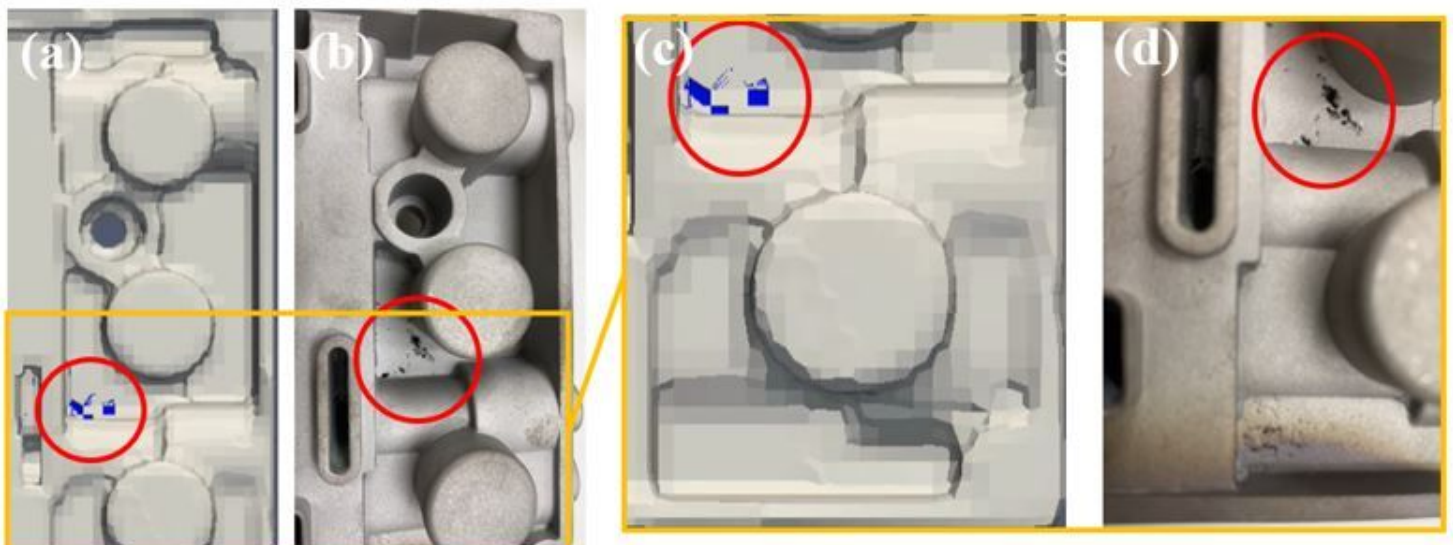


**Figure 14**

Simulation results of shrinking porosity on the surface (Case C) in the same position with actual casting. (a) PES in simulation model (b) photograph of trial casting with shrinkage porosity. (c) partial enlarge PES in simulation model (d) partial enlarge photograph of trial casting with shrinkage porosity

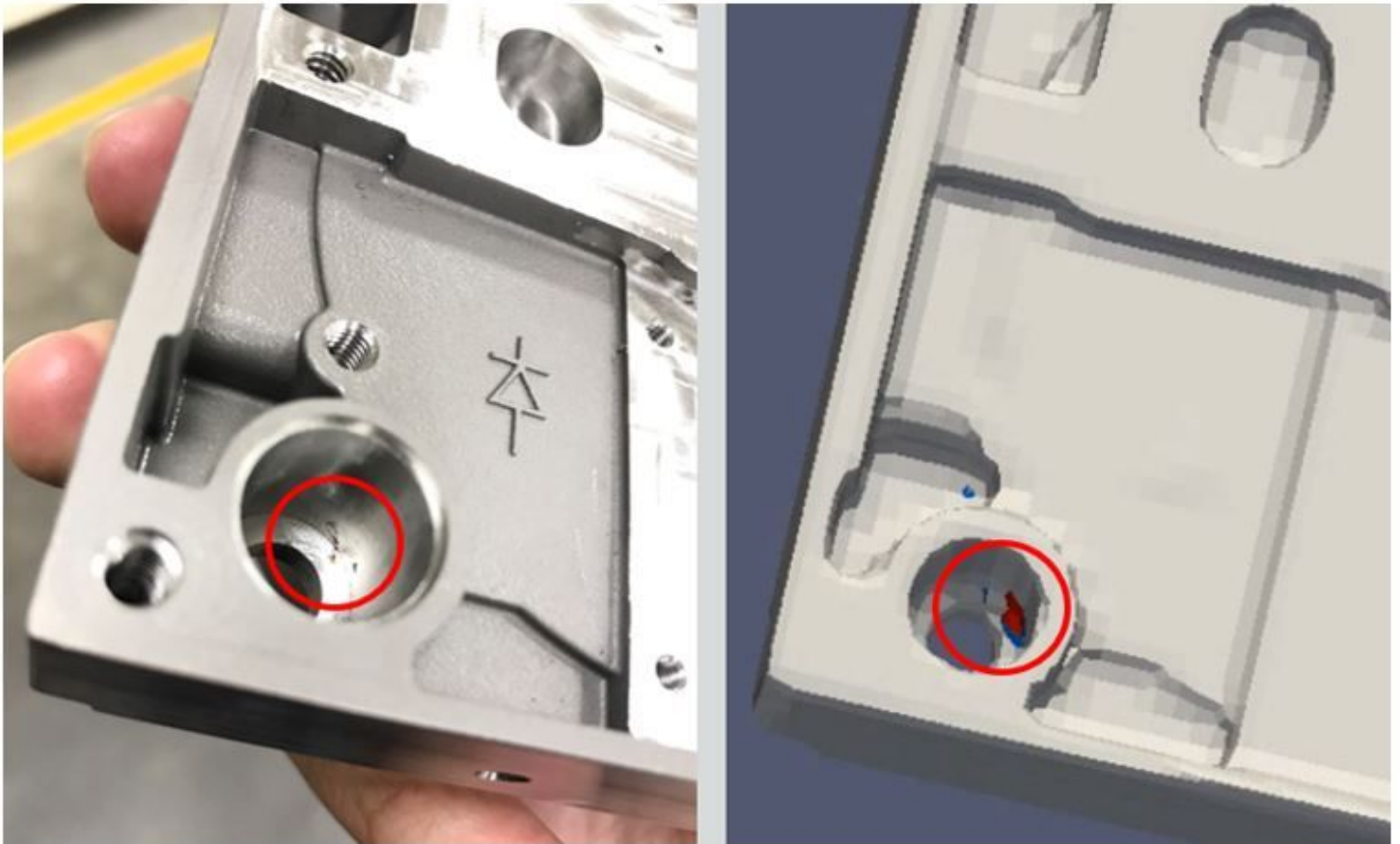


**Figure 15**

Simulation results of shrinking porosity on the inner side of the screw hole (Case C) in the same position as the actual casting photograph.

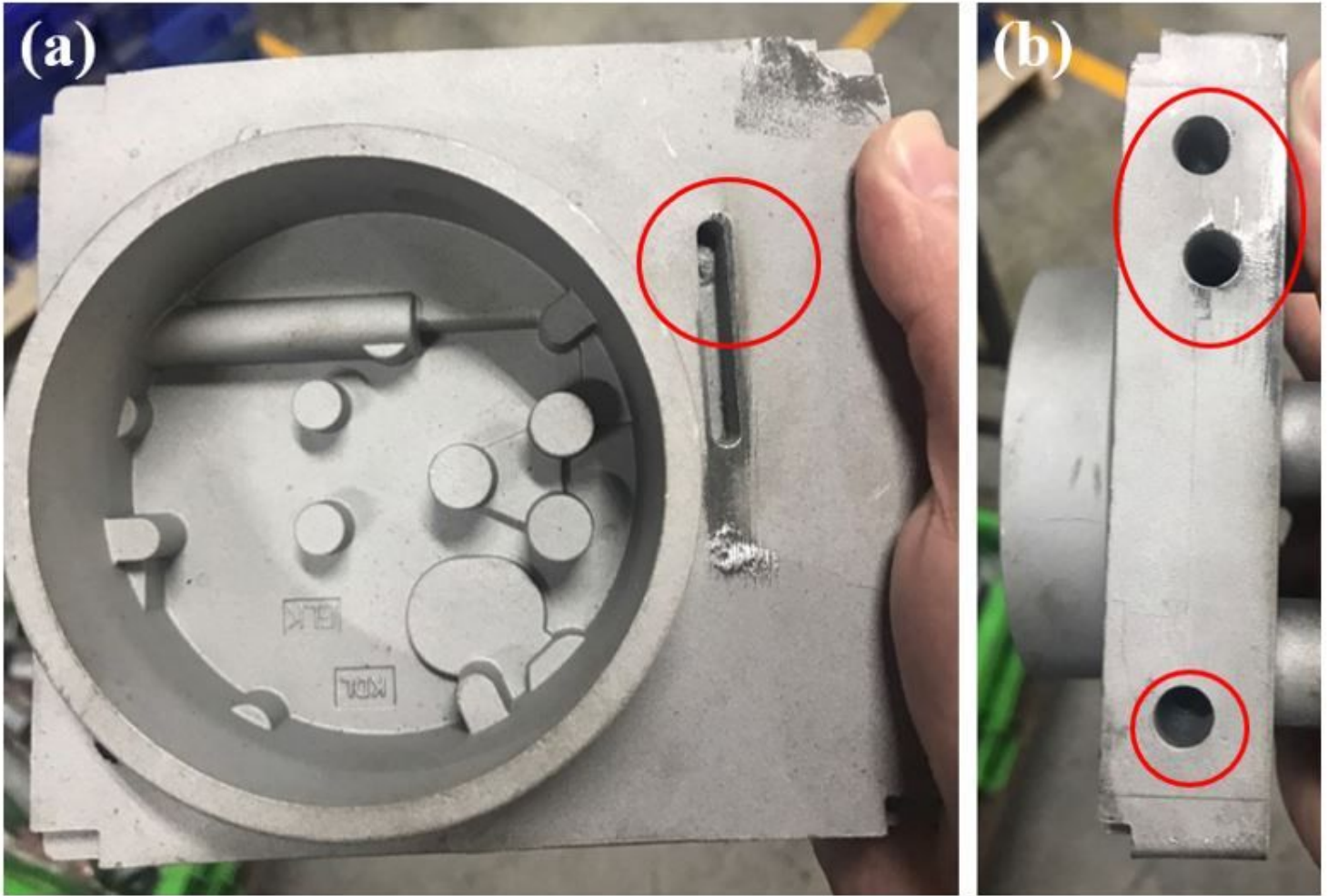
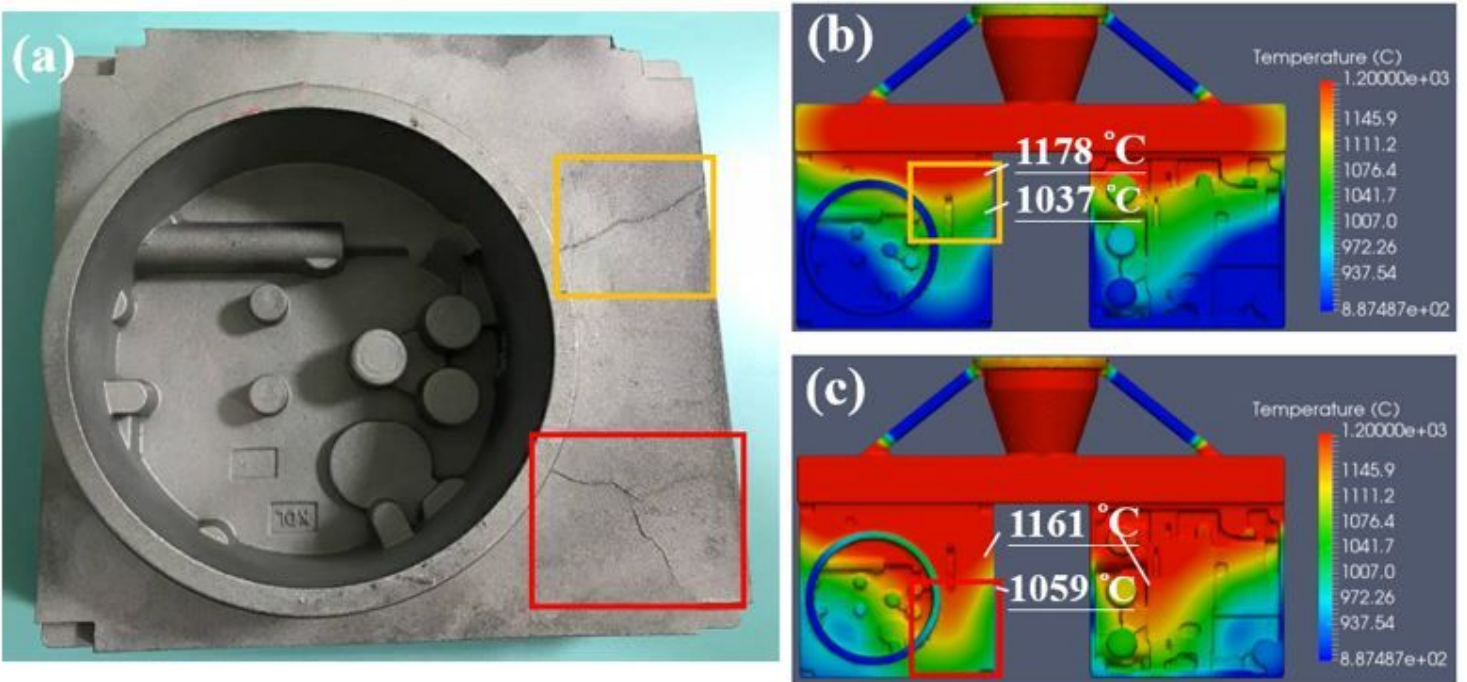


Figure 16

The ceramic core fracturing problem occurred on lots of trial casting in Case C and Case D.



**Figure 17**

Case D with wrinkled surface defects in trial casting. (a) real trial casting photograph. Corresponding the simulated results in different time steps (b) temperature of casting after pouring 645 sec. (c) the temperature of casting after pouring 364 sec.

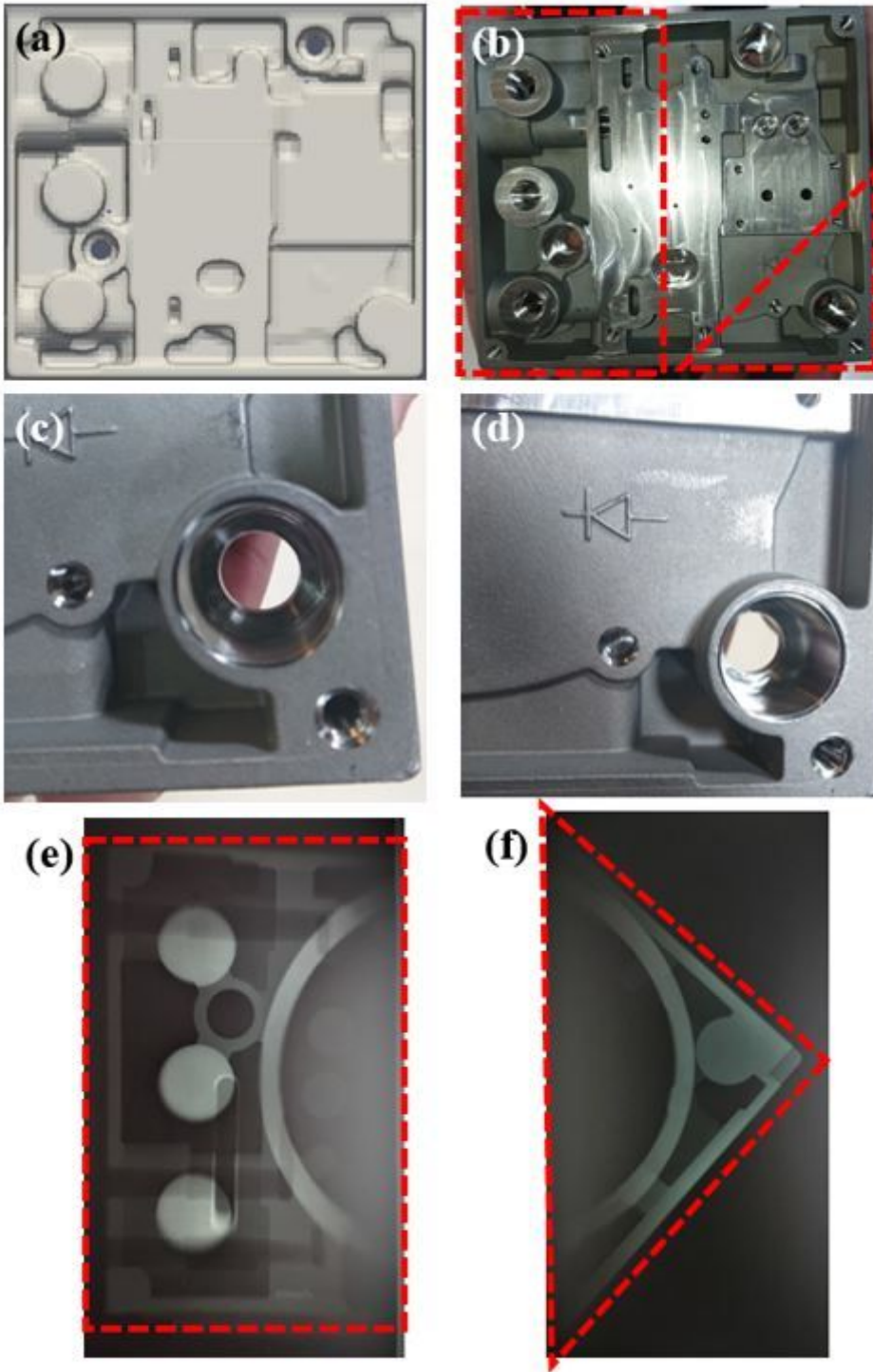
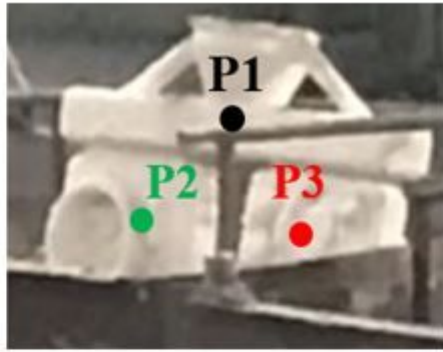


**Figure 18**

(a) Simulation results (b)(c)(d) images of actual casting (Case D). (e) X-ray images of the thick side of casting in Case D (f) X-ray images of screw hole which has shrinkage porosity in Case A and B but

perfect in Case D



GG02984 trial casting (Case D)

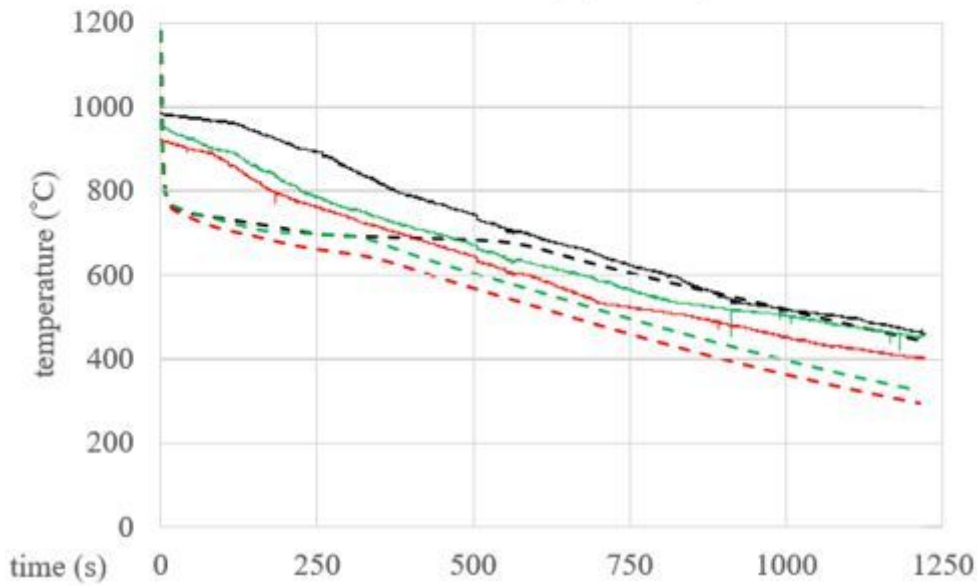
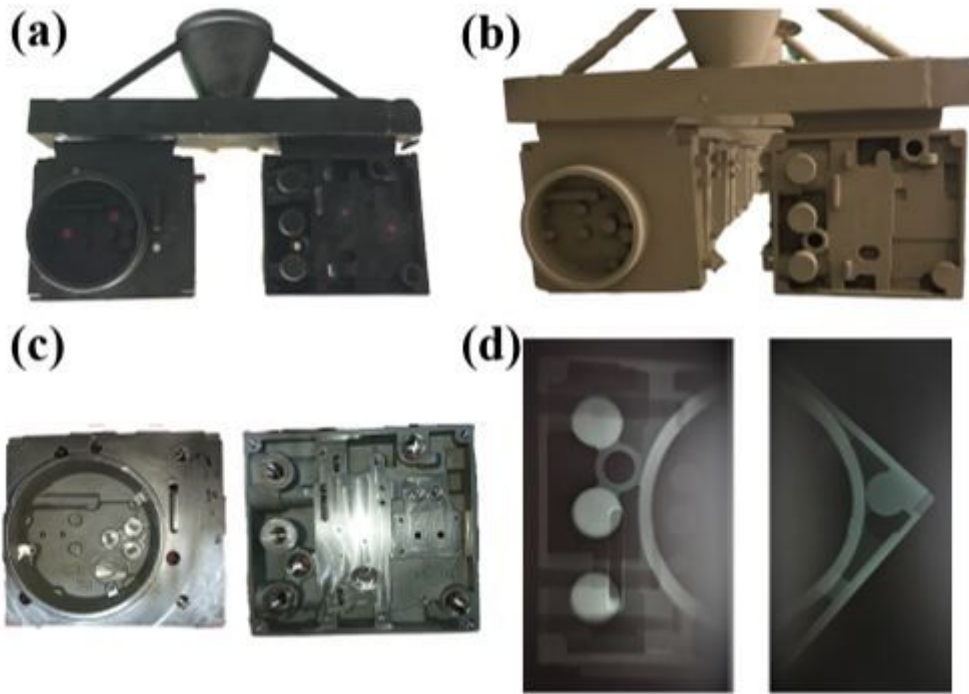


Figure 19

Case D shell mold temperature with time during the solidification process in three different positions, i.e., P1 in central of the runner, P2 in central of the front side of the casting shell mold, and P3 in central of the backside of the casting shell mold. Actual temperature measured with the thermal camera (solid line) and temperature predicted in simulation result (dotted line)



**Figure 20**

Images and X-ray photographs of casting in Case D. (a) Wax pattern. (b) a different view of ceramic shell mold with the die head. (c) Front view (left) and back view (right) of Case D casting. (d) cross-section of the product X-ray image